RESEARCH ARTICLE | FEBRUARY 14 2025

Electronic structure of YV_6Sn_6 probed by de Haas–van Alphen oscillations and density functional theory

Special Collection: Quantum Dynamics in Theory, Numerics and in Experimental Research

Kyryl Shtefiienko ; Cole Phillips; Shirin Mozaffari ; Richa P. Madhogaria; William R. Meier ; David G. Mandrus ; David E. Graf; Keshav Shrestha

APL Quantum 2, 016118 (2025)
https://doi.org/10.1063/5.0252563

Electronic structure of YV_6Sn_6 probed by de Haas–van Alphen oscillations and density functional theory

Cite as: APL Quantum 2, 016118 (2025); doi: 10.1063/5.0252563
Submitted: 10 December 2024 • Accepted: 27 January 2025 •
Published Online: 14 February 2025

Kyryl Shtefiienko,[1] Cole Phillips,[1] Shirin Mozaffari,[2] Richa P. Madhogaria,[2] William R. Meier,[2] David G. Mandrus,[2,3] David E. Graf,[4,5] and Keshav Shrestha[1,a)]

AFFILIATIONS

[1] Department of Chemistry and Physics, West Texas A&M University, Canyon, Texas 79016, USA
[2] Department of Materials Sciences and Engineering, University of Tennessee, Knoxville, Tennessee 37996, USA
[3] Materials Science & Technology Division, Oak Ridge National Laboratory, Oak Ridge, TN 37831, USA
[4] Department of Physics, Florida State University, Tallahassee, Florida 32306, USA
[5] National High Magnetic Field Laboratory, Tallahassee, Florida 32310, USA

Note: This paper is part of the APL Quantum Special Topic on Quantum Dynamics in Theory, Numerics and in Experimental Research.
[a)] **Author to whom correspondence should be addressed:** kshrestha@wtamu.edu or drkeshavshrestha@gmail.com

ABSTRACT

This study investigates the electronic structure of the vanadium-based kagome metal YV_6Sn_6 using magnetoresistance (MR) and torque magnetometry. The MR exhibits a nearly linear, non-saturating behavior, increasing by up to 55% at 35 T but shows no evidence of Shubnikov–de Haas oscillations. In contrast, the torque signal, measured up to 41.5 T, reveals clear de Haas–van Alphen (dHvA) oscillations over a wide frequency range, from a low frequency of F_α ~20 T to high frequencies between 8 and 10 kT. Angular and temperature-dependent dHvA measurements were performed to probe the Fermi surface parameters of YV_6Sn_6. The dHvA frequencies display weak angular dependence, and the effective mass, determined by fitting the temperature-dependent data to the Lifshitz–Kosevich formula, is 0.097 m_o, where m_o represents the free electron mass. To complement the experimental findings, we computed the electronic band structure and Fermi surface using density functional theory. The calculations reveal several notable features, including multiple Dirac points near the Fermi level, flatbands, and Van Hove singularities. Two bands cross the Fermi level, contributing to the Fermi surface, with theoretical frequencies matching well with the observed dHvA frequencies. These combined experimental and theoretical insights enhance our understanding of the electronic structure of YV_6Sn_6 and provide a valuable framework for studying other vanadium- and titanium-based kagome materials.

I. INTRODUCTION

Recently, kagome materials, with atomic arrangements resembling a corner-sharing kagome lattice, have attracted significant attention in condensed matter physics due to their fascinating properties, such as non-trivial topology, flatbands, charge-density wave (CDW), and superconductivity.[1–3] A prototypical example is AV_3Sb_5 (A = K, Rb, and Cs), also known as the "135" family, which forms a hexagonal lattice of V atoms coordinated by Sb atoms.[4–6] AV_3Sb_5 exhibits superconductivity with T_c ranging from ~0.3–3 K, CDW order near T_{CDW} ~80–110 K, and a Van Hove singularity, among other intriguing features.[7–10] Electronic band structure calculations reveal several remarkable properties, including the presence of flatbands, Van Hove singularity points, Dirac points near the Fermi level, and non-trivial $\mathbb{Z}_2$ topological invariants. Recent quantum oscillation studies[11–21] on AV_3Sb_5 have confirmed the non-trivial band topology and uncovered significant reconstruction of the Fermi surface in the CDW phase.

Another class of kagome compounds, RM_6X_6, known as the 166 family, has been discovered, where R represents alkali,

alkaline earth, or rare earth metals (e.g., Li, Mg, Yb, Sm, Gd, etc.); *M* represents transition metals (e.g., Co, Cr, Mn, V, Ni, etc.); and *X* represents Si, Ge, or Sn.[22–27] This family crystallizes in the $MgFe_6Ge_6$ prototype structure, exhibits significant chemical diversity, and, therefore, offers a wide range of functionalities. Several interesting physical phenomena have already been observed in this family, for example, a large anomalous Hall effect in $LiMn_6Sn_6$, non-trivial topological properties in GdV_6Sn_6,[24,28] Chern topological magnetism in $TbMn_6Sn_6$,[2] competing magnetic phases in YMn_6Sn_6,[29] and more. Notably, within this family, ScV_6Sn_6 is the only member to exhibit a CDW transition at T_{CDW} = 92 K.[30,31] However, no superconductivity has been observed in ScV_6Sn_6 under either ambient conditions or high pressures up to 11 GPa.[32] We recently reported on the electronic structure of ScV_6Sn_6, studied using high-field torque measurements[33] and density functional theory (DFT), which probed its electronic bands and Fermi surface, uncovering its non-trivial topology.

This work focuses on YV_6Sn_6, a member of the 166 kagome family. Figure 1(a) shows the unit cell (upper panel) and the kagome lattice (bottom panel) of vanadium atoms in YV_6Sn_6. Previous electrical transport and magnetic studies by Pokharel *et al.*[22] have shown that YV_6Sn_6 does not exhibit a magnetic transition or CDW order down to 2 K. Recent studies[34] suggest that the CDW phase in ScV_6Sn_6 originates from a structural instability caused by tin–tin bond modulation in the rare-earth–tin chains. This instability appears to be driven by the undersized scandium atoms, which allow the scandium–tin chains to rattle within the larger V–Sn framework. In contrast, yttrium is too large, preventing the rattling of the rare-earth–tin chain and inhibiting the development of a CDW phase in YV_6Sn_6. DFT studies[22] on this material have revealed a non-trivial band topology, confirmed by calculating the $\mathbb{Z}_2$ topological invariants. Here, we have investigated the electronic structure of YV_6Sn_6 by employing high-field torque measurements and DFT calculations. Torque measurements under applied fields of 41.5 T revealed well-defined de Haas–van Alphen (dHvA) oscillations with frequencies reaching up to 10 kT. DFT calculations of the electronic band structure show multiple Dirac points, Van Hove singularities, and flatbands near the Fermi level. A comparison of the theoretical frequencies derived from DFT with the experimental frequencies demonstrates good agreement.

II. EXPERIMENTAL AND COMPUTATIONAL DETAILS

High-quality single crystals of YV_6Sn_6 were synthesized via the tin flux method following the recipe in Refs. 34 and 35. Elemental Y (Alfa Aesar, 99.9%), V (Alfa Aesar, 99.8%), and Sn (Alfa Aesar, 99.9999%) were put in an alumina Canfield crucible set and then sealed in silica ampoules filled with about 0.2 atm argon. The ampoules were heated to 1150 °C over 12 h, held for 15 h, and cooled to 780 °C over 300 h. To remove the tin flux, the ampoules were centrifuged at 780 °C. To remove the remaining tin on the surface, the crystals were etched in an aqueous 10 wt. % HCl solution for 12–36 h. Temperature-dependent resistivity measurements were carried out in a physical property measurement system (Quantum Design) using the four-probe technique. Magnetoresistance (MR) and torque measurements with maximum applied magnetic fields up to 35 and 41.5 T, respectively, were carried out at the National High Magnetic Field Laboratory (NHMFL), Tallahassee, FL. Torque measurements were conducted using a miniature piezoresistive cantilever. A tiny single crystal of YV_6Sn_6 was selected and attached to the cantilever arm using vacuum grease and then mounted on a rotating platform of the measurement probe. The probe was slowly cooled down to a base temperature of 0.5 K. Two resistive elements on the cantilever were balanced at the base temperature before taking the field dependent and temperature dependent torque measurements. Magnetic fields were swept at each fixed temperature at a rate of 1.5 T/min.

Electronic structures were calculated using density functional theory (DFT) with the full-potential linearized augmented plane wave (FP-LAPW) method, as implemented in the WIEN2k code.[36] The exchange-correlation energies were treated using the standard generalized gradient approximation (PBE-GGA).[37] Internal atomic coordinates were optimized in the scalar relativistic mode until the forces on individual atoms were reduced to below 20 meV/Å. Spin–orbit coupling (SOC) was incorporated through the second variational step.[38] The energy convergence criterion for self-consistent calculations was set to 10^{-4} Ry. The atomic sphere radii (RMT) were chosen as 2.50 bohrs for Y, V, and Sn. Self-consistent calculations utilized a grid of 800 *k*-points across the full Brillouin zone, while a denser *k*-point mesh of 5000 points was employed for Fermi surface computations.

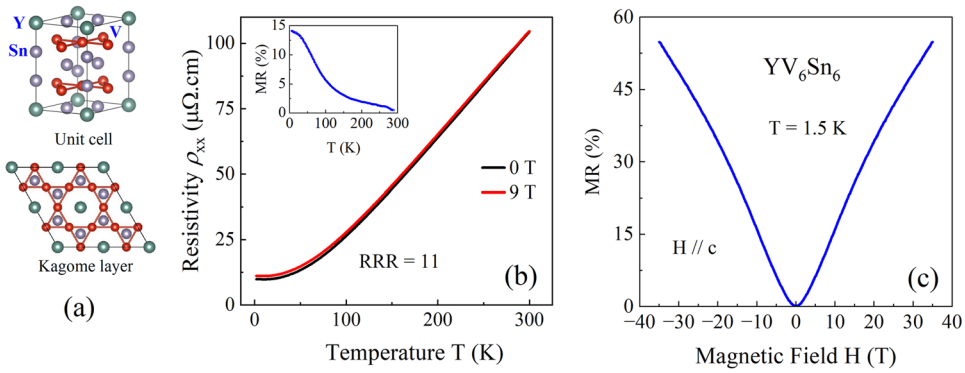

FIG. 1. (a) Unit cell (upper panel) and the top view (lower panel) of YV_6Sn_6, illustrating the kagome network formed by V atoms. (b) Temperature dependence of resistivity for a YV_6Sn_6 single crystal at 0 and 9 T. Inset: Magnetoresistance (MR) vs temperature plot. (c) MR plot for a YV_6Sn_6 single crystal with the magnetic field applied along the c-axis at T = 1.5 K. The MR reaches up to 55%, with no sign of quantum oscillations.

III. RESULTS AND DISCUSSION

Figure 1(b) shows the electrical resistivity, ρ_{xx}, as a function of temperature. As seen in the graph, the resistivity decreases with temperature, indicating typical metallic behavior. The residual resistivity ratio (RRR), calculated by dividing ρ_{xx} at 300 K by its value at 2 K, is 11, indicating the high quality of our YV_6Sn_6 crystals. Upon applying a magnetic field of 9 T, the resistivity increases, as shown by the red curve. The $\rho_{xx}(T)$ exhibits a similar behavior to that observed in another 166 family member, LuV_6Sn_6.[35] The inset displays the magnetoresistance (MR), defined as MR = $[\rho_{xx}\ (9\ \mathrm{T}) - \rho_{xx}(0)]/\rho_{xx}(0)$, where $\rho_{xx}(9\ \mathrm{T})$ and $\rho_{xx}(0)$ represent the resistivity values at 9 and 0 T, respectively. As shown in the inset, the MR reaches as high as 15% at 2 K and decreases to nearly zero at 300 K. In order to understand the effect of a magnetic field on electrical transport, we measured the electrical resistance as a function of the magnetic field. Figure 1(c) shows the MR for YV_6Sn_6 with the magnetic field applied along the c-axis at $T = 1.5$ K. As seen in the graph, the MR increases nearly linearly with the applied field, without any indication of saturation. At 35 T, the MR reaches 55%, but no Shubnikov–de Haas oscillations are observed. However, observing quantum oscillations is essential to probe the Fermi surface of YV_6Sn_6. Therefore, we proceed with an alternative measurement technique: torque magnetometry.

Figure 2(a) shows the τ vs field plot at two different tilt angles, $\theta = -7^\circ$ and -21°. Here, θ is defined as the angle between the magnetic field and the c-axis of the sample, as depicted in the upper inset of Fig. 2(a). The dHvA oscillations are clearly observed at both angles above 5 T. In addition to the low-frequency signal, there is an additional high-frequency signal at high magnetic fields above 30 T. The high-frequency signal is more prominent at $\theta = -7^\circ$ compared to $\theta = -21^\circ$, as indicated by the dotted circle. This is clearer in the zoomed-in plot of the high-field region, shown in the lower inset. To extract the oscillation frequencies, we subtracted a smooth polynomial background from the torque data and then performed a fast Fourier transform (FFT). Figure 2(b) shows the Fourier transform of the torque data presented in Fig. 2(a). The low-frequency component, $F_\alpha = 25$ T, is present at both angles, as shown in the inset. The torque signal at $\theta = -7^\circ$ exhibits additional frequencies at 180, 1400, and 8800 T. In contrast, at $\theta = -21^\circ$, these frequencies are completely overshadowed by the dominant lower frequency, F_α. Due to the low resolution of the high-frequency signal, it is difficult to extract from the torque data at some θ values. However, the lower frequency F_α is consistently observed at all measured angles. We observed a similar behavior in torque measurements[33] of another 166 compound, ScV_6Sn_6, where low frequencies are dominant and present at all θ values, while high frequencies are weak and only emerge at very high magnetic fields. This will be discussed in detail later.

In order to calculate the effective mass of charge carriers, we carried out the torque measurement at different temperatures. Figure 3(a) shows the temperature dependent torque data measured at $\theta = 28^\circ$. As seen in the graph, the dHvA oscillations are pronounced at low temperatures and gradually disappear at higher temperatures. At 35 K, the quantum oscillations are not visible. At this tilt angle, the lower frequency F_α changes to 18 T, and there is no interference from the high frequency signals, as seen in the frequency spectrum in Fig. 3(b). The amplitude of the frequency decreases at higher temperatures, and this behavior can be described by the Lifshitz–Kosevich (LK) theory.[39] According to the LK theory, the temperature dependent quantum oscillations in torque is given by

$$\Delta\tau(T,H) \propto e^{-\lambda_D}\frac{\lambda(T/H)}{\sin h[\lambda(T/H)]}, \tag{1}$$

with $\lambda_D(H) = \frac{2\pi^2 k_B}{\hbar e} m^* \frac{T_D}{H}$ and $\lambda(T/H) = \frac{2\pi^2 k_B}{\hbar e} m^* \frac{T}{H}$. Here, T_D, k_B, and m^* represent the Dingle temperature, Boltzmann's constant, and effective mass of the charge carriers, respectively. The first term is the Dingle factor, which describes the attenuation of the oscillations with decreasing field H. The second term explains the weakening of the oscillations at higher temperatures.

The inset in Fig. 3(b) shows the FFT amplitude at different temperatures. The scattered squares represent the FFT amplitude,

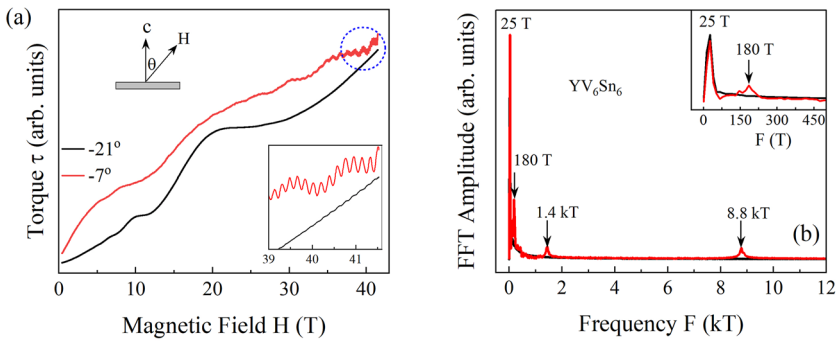

FIG. 2. (a) Torque (τ) of a YV_6Sn_6 single crystal measured up to 41.5 T at $\theta = -7^\circ$ and -21° and $T = 0.5$ K. The de Haas–van Alphen (dHvA) oscillations are observed at both angles above 5 T. A high-frequency signal is apparent at $\theta = -7^\circ$, as indicated by the dotted circle. Upper inset: A schematic diagram defining the tilt angle, θ. Lower inset: Zoomed-in torque data in the high-field region. The high-frequency signal is prominent at $\theta = -7^\circ$, although it is observed at both angles, -7° and -21°. (b) Frequency spectrum of the dHvA oscillations shown in (a). The low-frequency peak at $F_\alpha = 25$ T is present at both angles, while three additional frequencies, 180, 1400, and 8800 T, are observed only at $\theta = -7^\circ$. Inset: A zoomed-in view of the frequency spectrum highlighting the lower frequencies.

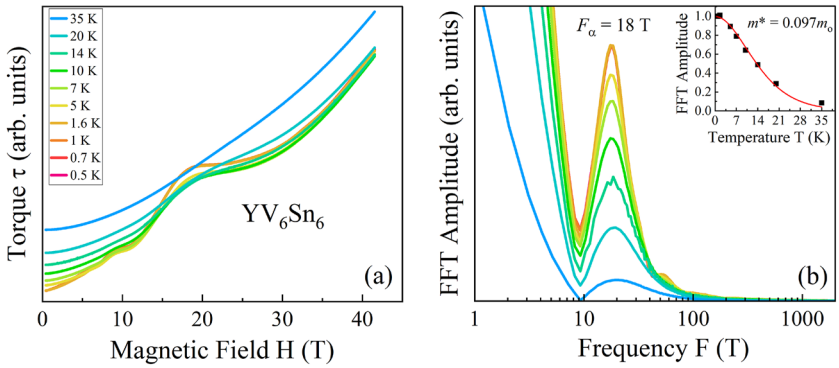

FIG. 3. Torque data of YV_6Sn6 at different temperatures. The de Haas–van Alphen (dHvA) oscillations are visible at low temperatures and gradually diminish at higher temperatures. (b) Frequency spectrum of the torque data shown in (a). A prominent peak is observed at F_α = 18 T in the frequency spectrum. Inset: temperature dependence of the frequency peak. The squares represent the data points, and the solid curve is the best fit using the Lifshitz–Kosevich formula.

while the solid red curve represents the best-fit curve to the data using the LK formula [Eq. (1)]. As shown in the graph, the LK formula explains the temperature-dependent behavior of the frequency. From the best fit, we determined $m^* = 0.097\ m_o$, where m_o is the rest mass of an electron. This m^* is comparable to the effective mass of other kagome systems[40,43–45] reported previously.

The angular dependence of quantum oscillations provides information about the shape, size, and dimensionality of the Fermi surface.[39,42–44] To explore this, we conducted torque measurements at various tilt angles. In Fig. 4(a), the torque data for YV_6Sn_6 measured at different θ values are shown. As shown in Fig. 4(a), there are clearly more than two periods, representing multiple quantum oscillation frequencies, and they seem to vary with θ values. Furthermore, the dHvA oscillations are present even if the magnetic field is perpendicular to the sample surface, indicating the three-dimensional nature of the Fermi surface. We have carried out background subtraction from the torque signal and determined the frequency values at different θ points, as presented in Fig. 4(b). For comparison purposes, we have also included possible theoretical frequencies computed by using DFT. We will discuss it in detail later.

From our high-field data, we observed a prominent peak at F_α, which appears to remain nearly constant while rotating the sample. In order to understand its topological feature, we calculated the Berry phase (Φ_B) of the Fermi pocket of F_α using the Landau level (LL) fan plot, as shown in Fig. S1 of the supplementary material. For a topologically non-trivial (or trivial) system, the Φ_B value is π (or zero).[42,45] To avoid possible interference from other frequency signals, we employed the FFT bandpass filter approach[21,40,46,47] to extract the oscillations corresponding to the particular frequency. When constructing this diagram, we assigned the LL index to the minima and maxima positions as $(N - \frac{1}{4})$ and $(N + \frac{1}{4})$, respectively.[46–48] By performing a linear extrapolation of the data, represented by the dashed line, we derived an intercept $N_0 = 0.18 \pm 0.02$, corresponding to $\Phi_B = (0.36 \pm 0.04)\pi$. Although Φ_B is not exactly π, its non-zero value indicates the non-trivial topology of the α pocket. Furthermore, the slope value (18.1 ± 0.3) T closely matches the F_α value of 18 T in Fig. 3(b), validating the precision of the linear extrapolation in determining the intercept (and consequently the Φ_B value). Furthermore, the bandpass filter's effectiveness in retaining the original dHvA oscillation signal without significant error is affirmed. A non-trivial Φ_B has been reported for the sister compound ScV_6Sn_6 using quantum oscillation studies.[33,49]

To better understand the experimental observations, we computed the electronic band structure and Fermi surface of YV_6Sn_6. Figure 5 illustrates the electronic band structures of YV_6Sn_6 (a) with-

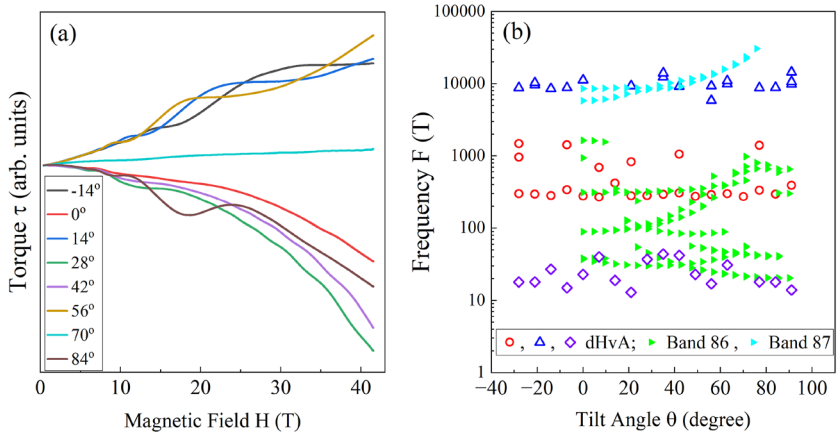

FIG. 4. (a) Angle-dependent torque signal for YV_6Sn_6. The period, and thus the frequency, of quantum oscillations varies with the tilt angle θ. (b) Comparison of theoretical frequencies from **band 86** and **band 87** with experimental quantum oscillation frequencies. **Band 86** frequencies align well with experimental values below 1000 T, while higher frequencies, around 10 kT, correspond closely to those from **band 87**.

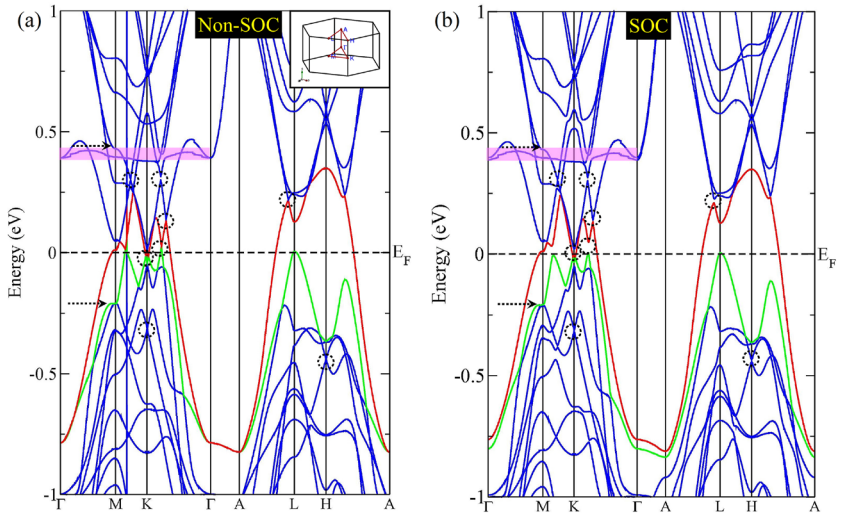

FIG. 5. Electronic band structure of pristine YV_6Sn_6 with (a) non-SOC and (b) SOC. The SOC is oriented along the [001] direction, corresponding to the out-of-plane axis of the material. The flatband is denoted by the shaded purple area, and the Dirac points near the Fermi level are indicated by the dotted circles. Two bands, indicated by red and green colors, cross the Fermi level. The dashed arrows represent the Van Hove singularities. Inset: first Brillouin zone showing high-symmetry points.

out and (b) with the inclusion of spin–orbit coupling (SOC). The inset in Fig. 5(a) shows the high-symmetry points in the first Brillouin zone. As shown in Fig. 5(a), the electronic bands exhibit several intriguing features, including multiple Dirac points near the Fermi level (highlighted by the dotted circles), a flatband (shaded area), and multiple Van Hove singularities (indicated by the dashed arrows). Orbital-resolved electronic band structure provides detailed insights into the contributions of specific atomic orbitals to the electronic bands in a material. This information is critical for understanding the electronic, magnetic, and optical properties of materials. Therefore, we computed the orbital-resolved electronic bands of YV_6Sn_6, as presented in Fig. S2 of the supplementary material. As shown in the graph, the electronic bands near the Fermi level are primarily dominated by the vanadium 3*d* orbitals. Moreover, features such as Dirac points, Van Hove singularities, and flatbands arise from the vanadium 3*d* and tin 5*p* orbitals. Notably, there appears to be no contribution from the yttrium 4*d* orbitals to the electronic bands of YV_6Sn_6.

Here, we have aligned the SOC along the [001] direction, corresponding to the out-of-plane axis of the material. To investigate the magnetic anisotropy, we calculated the effect of SOC along various directions, including [001], [100], [110], and [111]. Our analysis revealed that [110] is the easy axis for magnetization, while [001] is the hard axis. By computing the total energy differences between magnetization orientations along different crystallographic directions, we determined the magnetic anisotropy energy to be 0.23 meV for YV_6Sn_6.

Our electronic band structure is consistent with those calculated for other 166 kagome families.[22,33,41,50,51] With the inclusion of SOC, the electronic bands slightly shift (either up or down), as shown in Fig. 5(b). Here, the SOC is oriented along the [001] direction, corresponding to the out-of-plane axis of the material. While some of the Dirac points develop gaps due to the inclusion of SOC, the flatbands and Van Hove singularity points remain nearly intact. For example, the previously gapless Dirac point along the K–Γ and A–L directions develops a gap as high as ~50 meV in the presence of SOC. There are two bands: **band 86** and **band 87** cross the Fermi level, as indicated by the green and red colors, respectively. These bands contribute to the Fermi surface of YV_6Sn_6.

Figure 6 shows the band-resolved Fermi surface of YV_6Sn_6. The Fermi surface of **band 86** exhibits a chain-like feature at the Brillouin zone boundary, along with small pockets at the edge of the Brillouin zone. For **band 87**, there is a deformed, cylinder-like feature with a belly in the middle. The final inset represents the combined Fermi surface sheets from both bands. To understand the effect of SOC, we computed the Fermi surface of YV_6Sn_6 including the SOC effect, as shown in Fig. S3 of the supplementary material. It is found that the Fermi surface remains nearly unchanged. According to Onsager's relation,[39,42,52,53] the frequency (F) of quantum oscillations is directly proportional to the cross-sectional area (A_F) of the Fermi surface as $F = \hbar/(2\pi e)A_F{}^2$, where $\hbar$ is the reduced Planck constant and e is the charge of an electron. Therefore, we can calculate possible theoretical frequencies by measuring the cross-sectional area of the Fermi surface.

We employed the SKEAF code[54] for computing possible theoretical frequencies from the Fermi pockets derived from **band 86** and **band 87**. The calculated angular dependence of frequencies from different bands is plotted in Fig. 4(b) alongside the experimental data. As observed in the figure, frequencies derived from

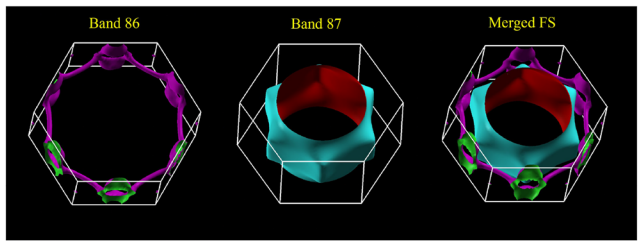

FIG. 6. Band resolved Fermi surface (FS) of YV_6Sn_6. Two bands: **band 86** and **band 87** contribute to the FS. The last inset is the combined FS sheets from both bands.

both **bands 86** and **87** describe the behavior of F_α. Low frequencies below 1000 T, observed in dHvA oscillations, are in good agreement with the theoretical frequencies computed from **band 86**. Similarly, the high-frequency signal near 10 kT is in good agreement with those computed from **band 87**. It is important to note that, although the frequency values are comparable, the angular dependence of the theoretical frequency derived from **band 87** shows an upward trend, especially above 60°, which is not clearly observed in the experimental data. The high frequency signal appears in very high fields (around 35 T) and is dominated by the low frequency signal, reducing its resolution [Figs. 4(a) and 2(a) and 2(b)]. This makes it challenging to track the angular dependence precisely. However, the angular dependence of the low frequencies is well captured by the frequencies derived from **band 86**. There are also possible frequencies below 100 T, but we did not observe these frequencies in our dHvA oscillation data. However, quantum oscillation experiments are not uncommon to miss higher frequencies.[55,56]

IV. SUMMARY

Despite the chemical diversity of 166 compounds, there are limited studies[33,41,49,50,57,58] that use quantum oscillations to understand their electronic properties. Moreover, most of these studies report the presence of low-frequency signals (below 100 T).[49,57,58] For instance, Ma *et al.* performed Shubnikov–de Haas (SdH) oscillations in RMn_6Sn_6 (R = Gd–Tm, Lu) and observed frequencies below 100 T. This paper focuses on the detailed electrical transport, magnetotransport, and torque magnetometry studies of YV_6Sn_6 with applied fields up to 41.5 T. Our electrical transport measurement shows that this material demonstrates a good metallic behavior. To investigate the magnetotransport properties, we measured magnetoresistance (MR) with the applied fields up to 35 T. We found nearly a linearly varying and non-saturating MR with the value reaching as high as 55%; however, there is no clear sign of SdH oscillations in MR data. Therefore, we proceeded with another measurement technique: torque magnetometry. Our torque data, measured up to 41.5 T, show clear de Haas–van Alphen (dHvA) oscillations with the major frequency near 20 T, along with a high frequency signal as high as 10 kT.

To probe the Fermi surface properties, we performed both angular and temperature-dependent torque measurements. To complement the experimental results, we calculated the electronic band structure and the Fermi surface of YV_6Sn_6 using density functional theory (DFT). The calculations reveal several Dirac points near the Fermi level, along with notable features such as flatbands and Van Hove singularities. Two electronic bands cross the Fermi level, contributing to the Fermi surface. Unlike other kagome materials, the Fermi surface consists of a deformed cylindrical pocket at the center and chain-like features along the boundary of the Brillouin zone. By analyzing the cross-sectional areas of these Fermi pockets, we computed theoretical dHvA frequencies, which show good agreement with the experimentally observed values.

We did not observe SdH oscillations in YV_6Sn_6 even at a maximum applied magnetic field of 35 T [Fig. 1(c)]. This is likely due to the sensitivity of resistivity-based SdH measurements to various damping effects, including electron–phonon interactions and scattering from defects and impurities within the crystal, which can suppress quantum oscillations. In contrast, torque magnetometry, which detects changes in magnetization, offers a higher signal-to-noise ratio and can amplify even subtle oscillations. Notably, torque measurements can resolve tiny high-frequency signals embedded within larger, low-frequency oscillations [Fig. 2(a)]. The proximity of multiple Dirac points near the Fermi level results in charge carriers behaving like massless Dirac fermions, characterized by exceptionally high mobility and unique quantum mechanical properties. As shown in Fig. 5, the flatband resides near the Fermi level (~0.4 eV above) and can be tuned closer through doping or application of external pressure. Furthermore, the presence of Van Hove singularities, or saddle points in the band structure where the density of states (DOS) diverges, significantly enhances electronic interactions, increasing the likelihood of emergent phenomena, such as magnetism, charge-density waves, and superconductivity. These combined experimental and computational insights presented here for YV_6Sn_6 provide a valuable foundation for understanding the electronic properties of other titanium- and vanadium-based kagome systems.

SUPPLEMENTARY MATERIAL

The supplementary material provides details on the Berry phase calculations (Fig. S1), orbital-resolved electronic band structures (Fig. S2), and band-resolved Fermi surfaces (Fig. S3) of YV_6Sn_6.

ACKNOWLEDGMENTS

The work at West Texas A&M University (WTAMU) was supported by the Killgore Undergraduate and Graduate Student Research Grants, the Welch Foundation (Grant No. AE-0025), and the National Science Foundation (Award No. 2336011). DFT calculations were performed in the WTAMU HPC cluster, which was funded by the National Science Foundation (NSF CC* GROWTH 2018841). S.M. and D.G.M. acknowledge the support from AFOSR MURI (Grant No. FA9550-20-1-0322) and the support from the Gordon and Betty Moore Foundation (Grant No. GBMF9069). A portion of this work was performed at the National High Magnetic Field Laboratory, which is supported by National Science Foundation Cooperative Agreement No. DMR-2128556 and the State of Florida.

AUTHOR DECLARATIONS

Conflict of Interest

The authors have no conflicts to disclose.

Author Contributions

K.S. and C.P. contributed equally to this work.

Kyryl Shtefiienko: Conceptualization (equal); Investigation (equal). **Cole Phillips**: Conceptualization (equal); Investigation (equal). **Shirin Mozaffari**: Conceptualization (equal); Investigation (equal). **Richa P. Madhogaria**: Conceptualization (equal); Investigation (equal). **William R. Meier**: Conceptualization (equal); Investigation

(equal). **David G. Mandrus**: Conceptualization (equal); Investigation (equal). **David E. Graf**: Conceptualization (equal); Investigation (equal). **Keshav Shrestha**: Conceptualization (lead); Formal analysis (equal); Investigation (lead); Writing – original draft (lead); Writing – review & editing (lead).

DATA AVAILABILITY

The data that support the findings of this study are available within the article.

REFERENCES

[1] L. Ye, M. Kang, J. Liu, F. von Cube, C. R. Wicker, T. Suzuki, C. Jozwiak, A. Bostwick, E. Rotenberg, D. C. Bell, L. Fu, R. Comin, and J. G. Checkelsky, Nature **555**, 638 (2018).

[2] J.-X. Yin, W. Ma, T. A. Cochran, X. Xu, S. S. Zhang, H.-J. Tien, N. Shumiya, G. Cheng, K. Jiang, B. Lian *et al.*, Nature **583**, 533 (2020).

[3] K. Jiang, T. Wu, J.-X. Yin, Z. Wang, M. Z. Hasan, S. D. Wilson, X. Chen, and J. Hu, Natl. Sci. Rev. **10**, nwac199 (2022).

[4] B. R. Ortiz, L. C. Gomes, J. R. Morey, M. Winiarski, M. Bordelon, J. S. Mangum, I. W. H. Oswald, J. A. Rodriguez-Rivera, J. R. Neilson, S. D. Wilson, E. Ertekin, T. M. McQueen, and E. S. Toberer, Phys. Rev. Mater. **3**, 094407 (2019).

[5] B. R. Ortiz, P. M. Sarte, E. M. Kenney, M. J. Graf, S. M. L. Teicher, R. Seshadri, and S. D. Wilson, Phys. Rev. Mater. **5**, 034801 (2021).

[6] B. R. Ortiz, S. M. Teicher, Y. Hu, J. L. Zuo, P. M. Sarte, E. C. Schueller, A. M. Abeykoon, M. J. Krogstad, S. Rosenkranz, R. Osborn, R. Seshadri, L. Balents, J. He, and S. D. Wilson, Phys. Rev. Lett. **125**, 247002 (2020).

[7] F. H. Yu, D. H. Ma, W. Z. Zhuo, S. Q. Liu, X. K. Wen, B. Lei, J. J. Ying, and X. H. Chen, Nat. Commun. **12**, 3645 (2021).

[8] K. Y. Chen, N. N. Wang, Q. W. Yin, Y. H. Gu, K. Jiang, Z. J. Tu, C. S. Gong, Y. Uwatoko, J. P. Sun, H. C. Lei, J. P. Hu, and J. Cheng, Phys. Rev. Lett. **126**, 247001 (2021).

[9] N. N. Wang, K. Y. Chen, Q. W. Yin, Y. N. N. Ma, B. Y. Pan, X. Yang, X. Y. Ji, S. L. Wu, P. F. Shan, S. X. Xu, Z. J. Tu, C. S. Gong, G. T. Liu, G. Li, Y. Uwatoko, X. L. Dong, H. C. Lei, J. P. Sun, and J.-G. Cheng, Phys. Rev. Res. **3**, 043018 (2021).

[10] M. Kang, S. Fang, J.-K. Kim, B. R. Ortiz, S. H. Ryu, J. Kim, J. Yoo, G. Sangiovanni, D. D. Sante, B.-G. Park, C. Jozwiak, A. Bostwick, E. Rotenberg, E. Kaxiras, S. D. Wilson, J.-H. Park, and R. Comin, Nat. Phys. **18**, 301 (2022).

[11] F. H. Yu, T. Wu, Z. Y. Wang, B. Lei, W. Z. Zhuo, J. J. Ying, and X. H. Chen, Phys. Rev. B **104**, 041103 (2021).

[12] Q. Yin, Z. Tu, C. Gong, Y. Fu, S. Yan, and H. Lei, Chin. Phys. Lett. **38**, 037403 (2021).

[13] S.-Y. Yang, Y. Wang, B. R. Ortiz, D. Liu, J. Gayles, E. Derunova, R. Gonzalez-Hernandez, L. Šmejkal, Y. Chen, S. S. P. Parkin, S. D. Wilson, E. S. Toberer, T. McQueen, and M. N. Ali, Sci. Adv. **6**, eabb6003 (2020).

[14] K. Nakayama, L. Yongkai, T. Kato, M. Liu, Z. Wang, T. Takahashi, Y. Yao, and T. Sato, Phys. Rev. X **12**, 011001 (2022).

[15] B. R. Ortiz, S. M. L. Teicher, L. K. abd Paul, M. Sarte, J. P. C. Ruff, R. Seshadri, and S. D. Wilson, Phys. Rev. X **11**, 041030 (2021).

[16] H. Luo, Q. Gao, H. Liu, Y. Gu, D. Wu, C. Yi, J. Jia, S. Wu, X. Luo, Y. Xu *et al.*, Nat. Commun. **13**, 273 (2022).

[17] Y. Fu, N. Zhao, Z. Chen, Q. Yin, Z. Tu, C. Gong, C. Xi, X. Zhu, Y. Sun, K. Liu, and H. Lei, Phys. Rev. Lett. **127**, 207002 (2021).

[18] W. Zhang, L. Wang, C. W. Tsang, X. Liu, J. Xie, W. C. Yu, K. T. Lai, and S. K. Goh, Phys. Rev. B **106**, 195103 (2022).

[19] C. Broyles, D. Graf, H. Yang, X. Dong, H. Gao, and S. Ran, Phys. Rev. Lett. **129**, 157001 (2022).

[20] K. Shrestha, M. Shi, T. Nguyen, D. Miertschin, K. Fan, L. Deng, D. E. Graf, X. Chen, and C.-W. Chu, Phys. Rev. B **107**, 075120 (2023).

[21] K. Shrestha, R. Chapai, B. K. Pokharel, D. Miertschin, T. Nguyen, X. Zhou, D. Y. Chung, M. G. Kanatzidis, J. F. Mitchell, U. Welp, D. Popović, D. E. Graf, B. Lorenz, and W. K. Kwok, Phys. Rev. B **105**, 024508 (2022).

[22] G. Pokharel, S. M. L. Teicher, B. R. Ortiz, P. M. Sarte, G. Wu, S. Peng, J. He, R. Seshadri, and S. D. Wilson, Phys. Rev. B **104**, 235139 (2021).

[23] J. Lee and E. Mun, Phys. Rev. Mater. **6**, 083401 (2022).

[24] S. Peng, Y. Han, G. Pokharel, J. Shen, Z. Li, M. Hashimoto, D. Lu, B. R. Ortiz, Y. Luo, H. Li, M. Guo, B. Wang, S. Cui, Z. Sun, Z. Qiao, S. D. Wilson, and J. He, Phys. Rev. Lett. **127**, 266401 (2021).

[25] E. Rosenberg, J. M. DeStefano, Y. Guo, J. S. Oh, M. Hashimoto, D. Lu, R. J. Birgeneau, Y. Lee, L. Ke, M. Yi, and J.-H. Chu, Phys. Rev. B **106**, 115139 (2022).

[26] X. Zhang, Z. Liu, Q. Cui, Q. Guo, N. Wang, L. Shi, H. Zhang, W. Wang, X. Dong, J. Sun, Z. Dun, and J. Cheng, Phys. Rev. Mater. **6**, 105001 (2022).

[27] G. Pokharel, B. Ortiz, J. Chamorro, P. Sarte, L. Kautzsch, G. Wu, J. Ruff, and S. D. Wilson, Phys. Rev. Mater. **6**, 104202 (2022).

[28] Y. Hu, X. Wu, Y. Yang, S. Gao, N. C. Plumb, A. P. Schnyder, W. Xie, J. Ma, and M. Shi, Sci. Adv. **8**, eadd2024 (2022).

[29] N. J. Ghimire, R. L. Dally, L. Poudel, D. Jones, D. Michel, N. T. Magar, M. Bleuel, M. A. McGuire, J. Jiang, J. Mitchell *et al.*, Sci. Adv. **6**, eabe2680 (2020).

[30] H. W. S. Arachchige, W. R. Meier, M. Marshall, T. Matsuoka, R. Xue, M. A. McGuire, R. P. Hermann, H. Cao, and D. Mandrus, Phys. Rev. Lett. **129**, 216402 (2022).

[31] T. Hu, H. Pi, S. Xu, L. Yue, Q. Wu, Q. Liu, S. Zhang, R. Li, X. Zhou, J. Yuan, D. Wu, T. Dong, H. Weng, and N. Wang, Phys. Rev. B **107**, 165119 (2023).

[32] X. Zhang, J. Hou, W. Xia, Z. Xu, P. Yang, A. Wang, Z. Liu, J. Shen, H. Zhang, X. Dong, Y. Uwatoko, J. Sun, B. Wang, Y. Guo, and J. Cheng, Materials **15**, 7372 (2022).

[33] K. Shrestha, B. Regmi, G. Pokharel, S.-G. Kim, S. D. Wilson, D. E. Graf, B. A. Magar, C. Phillips, and T. Nguyen, Phys. Rev. B **108**, 245119 (2023).

[34] W. R. Meier, R. P. Madhogaria, S. Mozaffari, M. Marshall, D. E. Graf, M. A. McGuire, H. W. S. Arachchige, C. L. Allen, J. Driver, H. Cao, and D. Mandrus, J. Am. Chem. Soc. **145**, 20943 (2023).

[35] S. Mozaffari, W. R. Meier, R. P. Madhogaria, N. Peshcherenko, S.-H. Kang, J. W. Villanova, H. W. S. Arachchige, G. Zheng, Y. Zhu, K.-W. Chen, K. Jenkins, D. Zhang, A. Chan, L. Li, M. Yoon, Y. Zhang, and D. G. Mandrus, Phys. Rev. B **110**, 035135 (2024).

[36] P. Blaha, K. Schwarz, G. K. Madsen, D. Kvasnicka, and J. Luitz, *An Augmented Plane Wave Plus Local Orbitals Program for Calculating Crystal Properties* (Schwarz, Vienna University of Technology, Austria, 2001), Vol. 60.

[37] J. P. Perdew, K. Burke, and M. Ernzerhof, Phys. Rev. Lett. **77**, 3865 (1996).

[38] K. Koepernik and H. Eschrig, Phys. Rev. B **59**, 1743 (1999).

[39] D. Shoenberg, *Magnetic Oscillations in Metals* (Cambridge University Press, 1984).

[40] C. Phillips, K. Shtefiienko, T. Nguyen, A. N. Capa Salinas, B. A. Magar, G. Pokharel, S. D. Wilson, D. E. Graf, and K. Shrestha, Phys. Rev. B **110**, 205135 (2024).

[41] C. Dhital, G. Pokharel, B. Wilson, I. Kendrick, M. M. Asmar, D. Graf, J. Guerrero-Sanchez, R. Gonzalez-Hernandez, and S. D. Wilson, Phys. Rev. B **109**, 235145 (2024).

[42] B. R. Ortiz, P. M. Sarte, E. M. Kenney, M. J. Graf, S. M. L. Teicher, R. Seshadri, and S. D. Wilson, Phys. Rev. Mater. **5**, 034801 (2021).

[43] K. Shrestha, V. Marinova, D. Graf, B. Lorenz, and C. W. Chu, Phys. Rev. B **95**, 075102 (2017).

[44] K. Shrestha, D. Graf, V. Marinova, B. Lorenz, and C. W. Chu, J. Appl. Phys. **122**, 125901 (2017).

[45] K. Shrestha, "Magnetotransport studies on topological insulators," Doctoral dissertation, University of Houston (2015), see https://hdl.handle.net/10657/4881.

[46] T. Nguyen, N. Aryal, B. K. Pokharel, L. Harnagea, D. Mierstchin, D. Popović, D. E. Graf, and K. Shrestha, Phys. Rev. B **106**, 075154 (2022).

[47] K. Shrestha, M. Shi, B. Regmi, T. Nguyen, D. Miertschin, K. Fan, L. Z. Deng, N. Aryal, S.-G. Kim, D. E. Graf, X. Chen, and C. W. Chu, Phys. Rev. B **107**, 155128 (2023).

[48] K. Shrestha, D. Miertschin, R. Sankar, B. Lorenz, and C. W. Chu, J. Phys.: Condens. Matter **33**, 335501 (2021).

[49]G. Zheng, Y. Zhu, S. Mozaffari, N. Mao, K.-W. Chen, K. Jenkins, D. Zhang, A. Chan, H. W. S. Arachchige, R. P. Madhogaria *et al.*, J. Phys.: Condens. Matter **36**, 215501 (2024).
[50]E. Rosenberg, J. M. DeStefano, Y. Lee, C. Hu, Y. Shi, D. Graf, S. M. Benjamin, L. Ke, and J.-H. Chu, Phys. Rev. B **110**, 035119 (2024).
[51]S. R. Bhandari, M. Zeeshan, V. Gusain, K. Shrestha, and D. Rai, APL Quantum **1**, 046118 (2024).
[52]K. Shrestha, V. Marinova, B. Lorenz, and P. C. W. Chu, Phys. Rev. B **90**, 241111 (2014).
[53]K. Shrestha, V. Marinova, B. Lorenz, and C. W. Chu, J. Phys.: Condens. Matter **30**, 185601 (2018).
[54]P. Rourke and S. Julian, Comput. Phys. Commun. **183**, 324 (2012).
[55]W. Zheng, R. Schönemann, S. Mozaffari, Y.-C. Chiu, Z. B. Goraum, N. Aryal, E. Manousakis, T. M. Siegrist, K. Wei, and L. Balicas, Phys. Rev. B **102**, 125103 (2020).
[56]D. Rhodes, R. Schönemann, N. Aryal, Q. Zhou, Q. R. Zhang, E. Kampert, Y.-C. Chiu, Y. Lai, Y. Shimura, G. T. McCandless, J. Y. Chan, D. W. Paley, J. Lee, A. D. Finke, J. P. C. Ruff, S. Das, E. Manousakis, and L. Balicas, Phys. Rev. B **96**, 165134 (2017).
[57]W. Ma, X. Xu, J.-X. Yin, H. Yang, H. Zhou, Z.-J. Cheng, Y. Huang, Z. Qu, F. Wang, M. Z. Hasan, and S. Jia, Phys. Rev. Lett. **126**, 246602 (2021).
[58]M. He, X. Xu, D. Li, Q. Zeng, Y. Liu, H. Zhao, S. Zhou, J. Zhou, and Z. Qu, Phys. Rev. B **109**, 155117 (2024).